

We are IntechOpen, the world's leading publisher of Open Access books Built by scientists, for scientists

5,300

Open access books available

130,000

International authors and editors

155M

Downloads

Our authors are among the

154

Countries delivered to

TOP 1%

most cited scientists

12.2%

Contributors from top 500 universities



WEB OF SCIENCE™

Selection of our books indexed in the Book Citation Index
in Web of Science™ Core Collection (BKCI)

Interested in publishing with us?
Contact book.department@intechopen.com

Numbers displayed above are based on latest data collected.
For more information visit www.intechopen.com



Stabilizing Zero-Field Skyrmions at Room-Temperature in Perpendicularly Magnetized Multilayers

Jeovani Brandão, Marcos Vinicius Puydinger dos Santos and Fanny Béron

Abstract

Magnetic skyrmions are twirling spin structures observed in bulk, thin films, and multilayers with several features for both fundamental physics understanding and spintronic applications, i.e., nanoscale size, efficient transport under electrical current, and topological protection against defects. However, most magnetic skyrmions have been observed under the assistance of an out-of-plane magnetic field, which may limit their use in magnetic memory technologies. In this chapter, we review and present two recent mechanisms to create zero-field skyrmions at room-temperature in ferromagnetic multilayers. First, by tuning the perpendicular magnetic anisotropy (PMA) and remnant magnetization (near magnetization saturation) in unpatterned symmetric multilayer systems, it was achieved a transition from worm-like domains to isolated skyrmions. Besides, we present how to find stable zero-field skyrmions in arrays of ferrimagnetic discs by tailoring their diameter. Both methods demonstrate a robust route to stabilize zero-field skyrmions at room temperature, thus providing an important contribution to possible applications of these textures in the next generation of skyrmionics devices.

Keywords: multilayers, room-temperature, stability, skyrmions, zero-field

1. Introduction

Chiral magnets [1–8] have been investigated intensively in the last years due to their fascinating physical concepts and potential use in applications including sensors [9–11], logic [12–14], and magnetic memory devices [15, 16]. Among different magnetic structures, domain walls [17], vortices [18], and skyrmions [19] have been investigated both theoretically and experimentally. They exhibit remarkable static and dynamic behaviors under external stimulation such as magnetic [20] and electrical fields [21], thermal effects [22], and electrical currents [23]. More specifically, magnetic skyrmions, i.e., small-sized non-collinear chiral spin textures [24], have been attracted much attention as the favorable candidates for information storage in different technological devices, as examples, racetrack memories designed as nanowires [25] and nano-oscillators [26] based on confined nano-discs [27]. This

huge interest in manipulating skyrmions lies in their special properties including topological protection [28], efficient transport under low electric current density [29], and reduced (below 100 nm) size [30].

Experimentally, these non-collinear spin structures were firstly observed a little more than one decade ago in bulk systems [31], but at low temperatures (around 30 K) and under magnetic fields (around 0.2 T) [32, 33]. To achieve skyrmions at ambient conditions, perpendicularly magnetized multilayers made of nano-thick magnetic and non-magnetic materials have been used as a platform with suitable parameters to host skyrmions at room-temperature [20]. One important parameter is the Dzyaloshinskii-Moriya interaction (DMI) induced by spin orbit-coupling [34]. In the case of multilayers, it arises due to the interfacial nature between the atoms of the heavy metal (HM)\ferromagnetic (FM) layers [20]. The DMI is responsible for the chirality of the magnetic structure, i.e., the direction in which the spins rotate in the texture, giving rise to the topological skyrmion stability [6].

For multilayers made of thin films, such as Pt/Co/Ta, Pt/Co/Ir, Pt/Co/W, and other combinations, skyrmions have been observed in most cases under applied external magnetic fields [20, 35, 36], while at zero magnetic field the magnetic ground state favors the formation of spin spirals or labyrinthine magnetic configurations [37]. Under the assistance of a moderate magnetic field, the magnetic stripes shrink into small circular structures [20, 35], leading to the creation of magnetic skyrmions. This is possible thanks to the DMI that acts to protect the skyrmion against collapsing into a uniform magnetic state [20]. Moreover, the skyrmion size depends on the magnetic field strength, usually being inversely proportional to the applied field [20, 38].

This mechanism for creating skyrmions in multilayers under the aid of a magnetic field opened an avenue for controlling their fundamental physical properties such as size and density. On the other hand, the usage of skyrmions in the next generation of magnetic memory devices will depend on the achievement of skyrmions without the support of external stimuli. In this sense, the research for efficient methods to establish zero-field skyrmions at room-temperature yields interesting findings. For instance, zero-field skyrmions have been observed at room-temperature in lithographically shaped squares [39], through an exchange bias-field created at the interface of antiferromagnetic/ferromagnetic-based structures [40], and by their direct writing using magnetic force microscopy (MFM) tips [41], X-rays [42], and electron beam [43].

In this chapter, we report on two current processes for stabilizing zero-field magnetic skyrmions in ferro- and ferrimagnetic multilayers at ambient conditions. The different approaches driving the formation of zero-field skyrmions consist of tuning the magnetic properties such as perpendicular magnetic anisotropy (PMA) and DMI in unpatterned symmetric multilayers, as well as by tailoring the geometric size of circular discs. The zero-field skyrmions were imaged by magnetic force microscopy at room-temperature. Both mechanisms establish efficient strategies to create zero-field skyrmions at ambient conditions, which is an important advance in the development of skyrmionics devices.

2. Zero-field Skyrmions in Unpatterned symmetric multilayers

Skyrmions at room-temperature are created in perpendicularly magnetized multilayers made of a magnetic material sandwiched by two different heavy metal layers, HM1 and HM2, which yield sizeable DMI values to topologically protect and stabilize skyrmions under the assistance of a magnetic field [20]. Therefore,

most previous works have focused on asymmetric multilayers, which, at zero field and under the competition of different energies (exchange, anisotropy, dipolar, DMI), can lead to the labyrinthine domain structures. These domain structures turn into skyrmions in the presence of a magnetic field below the saturation magnetization [20, 35, 36].

Alternatively, symmetric multilayers made of the same heavy metal layers, for instance Pt/Co/Pt and Pd/Co/Pd, can also be used to create skyrmions [44]. It has been demonstrated that for polycrystalline symmetric Pt/Co/Pt tri-layers deposited by magnetron sputtering, a low but non-negligible DMI is measurable in the system [45]. More recently, a strong DMI has been observed in symmetric Pd/Co superlattices grown by molecular beam epitaxial (MBE) technique [46]. This is due to the differences in the crystalline structures and inhomogeneities at the interfaces of the HM/FM and FM/HM layers, which yield to the formation of asymmetric interfaces. Therefore, a DMI emerges in these irregular interfaces and opens the possibility for exploring chiral magnetic textures in symmetric systems [47].

In this sense, in order to find zero-field skyrmions at room-temperature, multilayers of (Pd/Co/Pd) \times 15 were fabricated by magnetron sputtering technique, where the Pd thickness was fixed at 2 nm and the Co layer varied from 0.2 to 0.8 nm.

Figure 1 shows the schematic representation of the multilayer Pd/Co/Pd grown on Si/SiO₂ substrate.

2.1 Magnetic properties

Hysteresis loops acquired under out-of-plane magnetic field for different Co thicknesses show that the reversal magnetization behavior depends on the Co thickness (**Figure 2**). At 0.8 nm-thick Co (down blue triangles), the hysteresis loop exhibits a very low remnant magnetization, while its saturation occurs beyond 150 mT, which is a larger magnetic field compared to the ones obtained for thicknesses below 0.8 nm. It essentially means that for this specific thickness, the in-plane anisotropy plays an important role in the magnetization reversal. It has already been demonstrated that above this thickness (0.8 nm thick Co), the magnetization of a similar multilayered system lies in the sample plane [48].

Moreover, by reducing the Co layer thickness to 0.6 nm, the hysteresis loop turns into a tail-like shape with reduced saturation magnetic field (up green triangles), but no significant change is observed for the remnant magnetization. This tendency is altered significantly when the Co thickness is reduced to 0.4 (red circles) and 0.2 nm (black squares). The square format of the magnetization curve is characterized by a reduction of the saturation magnetic field, as well as a notable enhancement of the remnant magnetization (near to the saturation magnetization),

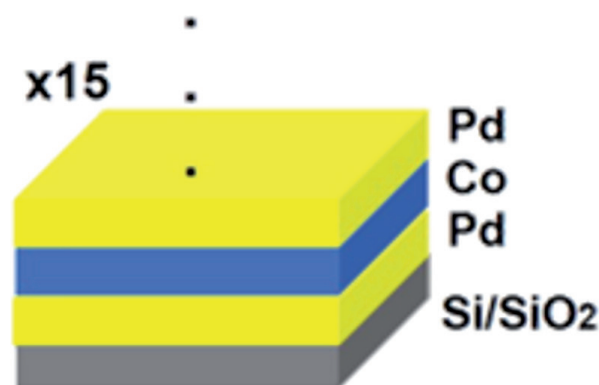


Figure 1. Stack of the symmetric multilayer produced by magnetron sputtering. Figure adapted from reference [47].

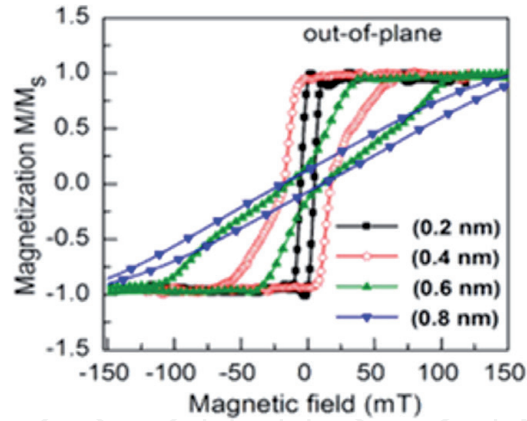


Figure 2. Out-of-plane hysteresis curves for different Co thicknesses. Figure adapted from reference [47].

indicating that the (PMA) is higher in this thickness range. It yields a thickness-dependency modulation of the remnant magnetization.

Consequently, both the tunable remnant magnetization and the PMA as a function of the thickness play an important role in the resulting magnetic domain patterns at zero magnetic field and room-temperature, as shown in **Figure 3**. The blue frame (0.8 nm) exhibits the formation of small periodic out-of-plane magnetic domains, while the green frame (0.6 nm), of the well-known worm-like domain pattern in such perpendicularly magnetized systems. The domain pattern transition occurs at Co-thick 0.4 nm (red frame), where the MFM image shows long separated magnetic stripes with a few circular domains in between. This is a preliminary indication of the magnetic skyrmion formation in the symmetric multilayer.

The formation of these round structures in symmetric multilayers is further confirmed for the 0.2 nm-thick Co film (black frame), in which the magnetic domain pattern is given by isolated skyrmions at room-temperature and zero magnetic field. This result shows that by carefully tuning the remnant magnetization and PMA of the multilayer, isolated skyrmions can be observed without the need of applying a magnetic field. In other words, increasing the PMA and the remnant magnetization can yield the formation of field-free skyrmions at ambient conditions. Notably, these skyrmions are created only by tuning the multilayer thickness, rather than through any geometric confinement or writing methodologies. This represents a straightforward and feasible alternative to stabilize zero-field skyrmions at room-temperature.

2.2 Skyrmion formation reproducibility

The homogeneity of the magnetic skyrmions along the sample surface was also tracked by taking MFM images over different areas of the 0.2 nm-thick Cofilm, as shown in **Figure 4**. The skyrmions are isolated with randomly distributed positions. This result confirms that the skyrmions at zero-field are reproducible on the entire surface of the multilayer rather than from any topographic influence on the different sample regions. Besides, the skyrmion sizes observed in each image are slightly different, which arises from minor inhomogeneities in the sample and different local variations of the multilayer properties such as saturation magnetization (M_s), PMA, and DMI [49].

To explore the features of the stabilized zero-field skyrmions, their size (diameter) and density (number of skyrmions per area) were extracted from the MFM

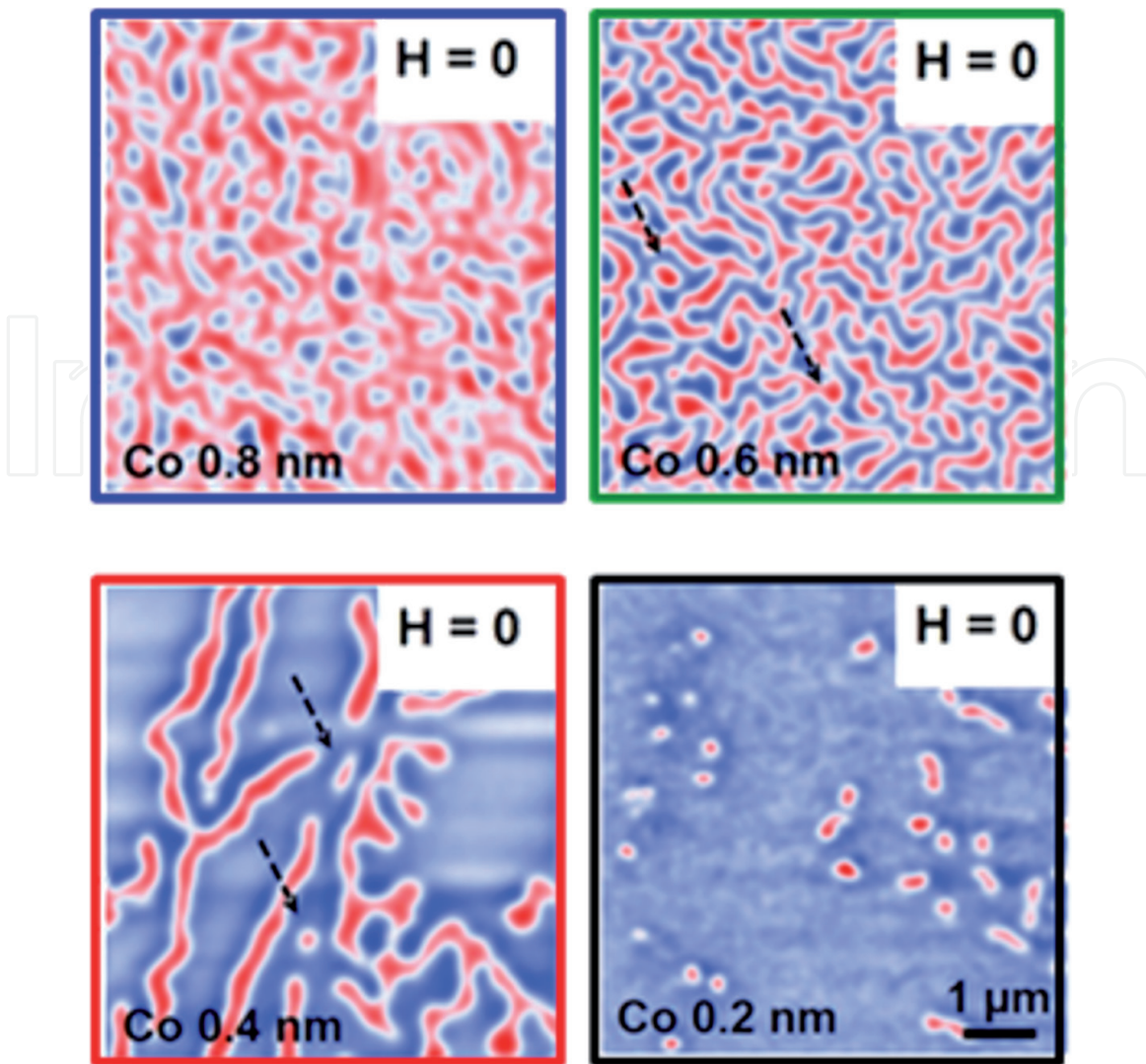


Figure 3. Magnetic force microscopy (MFM) images of the zero-field domain evolution. Figure adapted from reference [47].

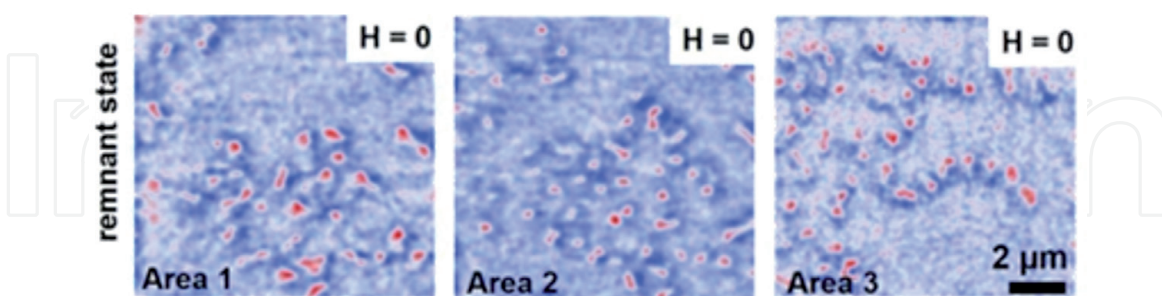


Figure 4. Magnetic skyrmions observed in different areas of the 0.2 nm-thick Co film at the remnant state. Figure adapted from [47].

images. The skyrmion size was evaluated by performing line scans on the magnetic structures and using the full width at half maximum (FWHM), as shown in **Figure 5(a)** and compiled in a histogram in **Figure 5(b)**, along with the skyrmion density statistics (**Figure 5(c)**). The average size and density of the skyrmions were $\sim 165 \text{ nm} \pm 32 \text{ nm}$ and $0.25/\mu\text{m}^2$. These values agree with previous works where skyrmions were stabilized under applied magnetic field [20, 35], which usually reduces these values [37].

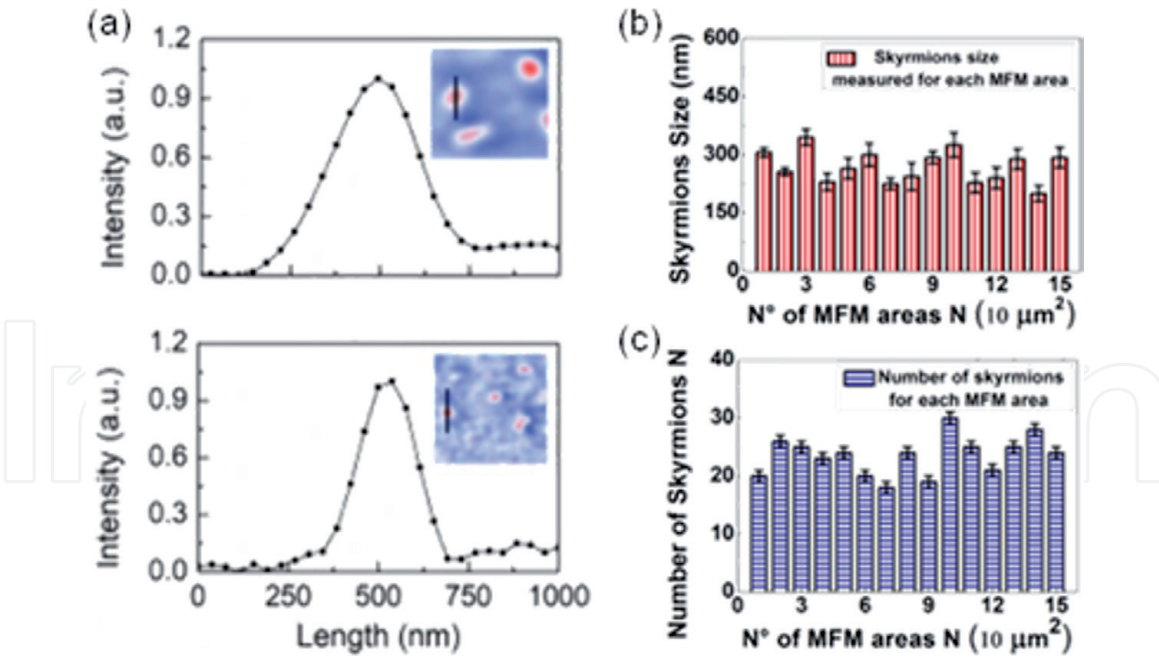


Figure 5. (a) Line scans performed on skyrmions of different sizes. Histograms of the skyrmion size (b) and number (c) distributions obtained in each MFM image. Figure adapted from [47].

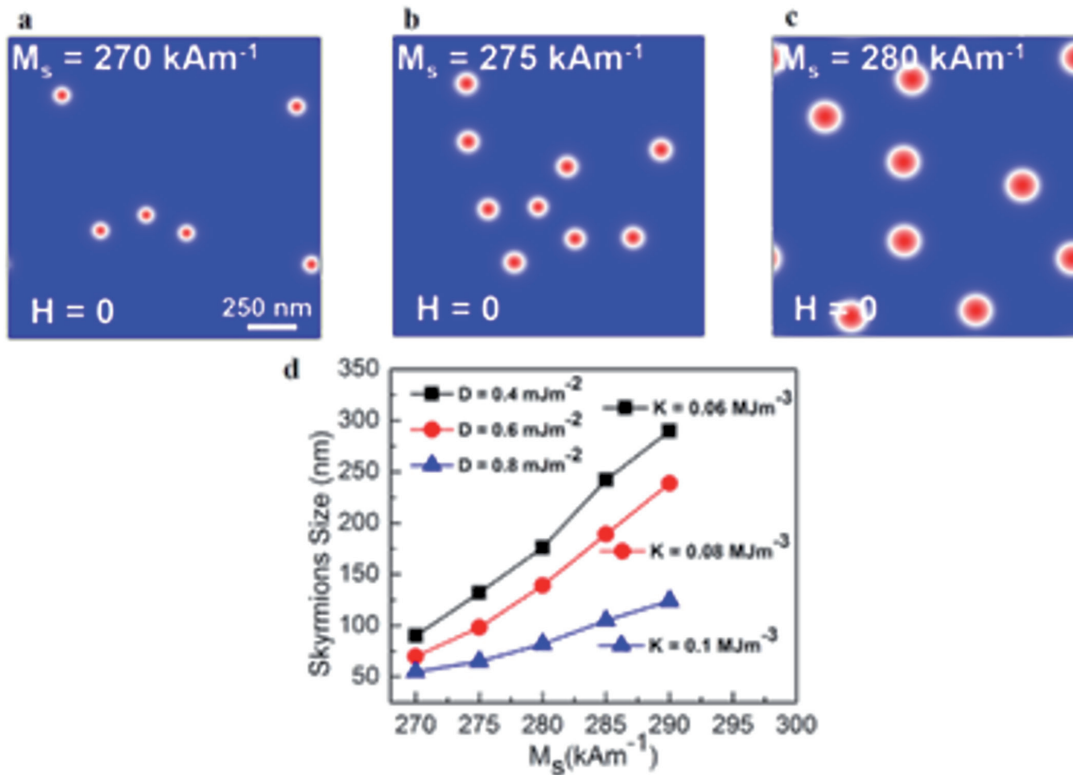


Figure 6. (a-c) Micromagnetic results of isolated skyrmions stabilized at zero magnetic field. (d) Skyrmion size obtained as a function of M_s for different values of PMA and DMI. Figure taken from [47].

2.3 Micromagnetic simulations

The formation of zero-field skyrmions in unpatterned symmetric multilayers is described better with the assistance of micromagnetic simulations. Mumax3 was the chosen code to carry out the simulations, and the used methods and parameters can be found in [47]. The results are summarized in **Figure 6**.

In **Figures 6(a-c)**, the micromagnetic simulations are representative for an anisotropy $K = 0.06 \text{ MJm}^{-3}$ and a Dzyaloshinskii-Moriya interaction $D = 0.04 \text{ mJm}^{-2}$, while the saturation magnetization M_s was varied. It shows that skyrmions are stabilized at zero-field with a random distribution of their positions, corroborating our experimental findings. Furthermore, by varying D in the micromagnetic simulations and comparing with the size of zero-field skyrmions obtained experimentally, the DMI was estimated to range between $0.4\text{--}0.8 \text{ mJm}^{-2}$. More details can be seen in the phase diagrams shown in the next section.

More remarkable, the skyrmion size increases for larger values of M_s as clearly shown in **Figures 6(a-c)**, indicating that this parameter plays an important role on the skyrmion diameter due to the impact of the magnetization stray field upon the magnetic structure size. In addition to the saturation magnetization, the influence of both K and D parameters was evaluated to understand their effects on the skyrmion stability and size. Figure 6 (d) shows that the skyrmion size monotonically increases as a function of M_s for any value of K and D . However, smaller K and D values lead to larger skyrmion size (black squares) compared to higher values (red circles and blue triangles). This important conclusion suggests that the sample saturation magnetization M_s must be reduced, while the PMA and DMI must be increased slightly to reduce the skyrmion average size at zero-field. This can be accomplished by engineering the multilayer structure varying, for instance, the magnetic layer thickness.

2.4 Magnetic domain phase diagrams

A phase diagram was constructed using the micromagnetic simulations to explore and indicate the achievable magnetic ground states as a function of the multilayer magnetic parameters, as can be seen in **Figure 7**.

Three different magnetic ground states were acquired at zero magnetic field, as shown in **Figure 7(a)**: uniform magnetization (dark cyan frame), isolated skyrmions (cyan frame), and mixed phase (purple frame), in which the latter

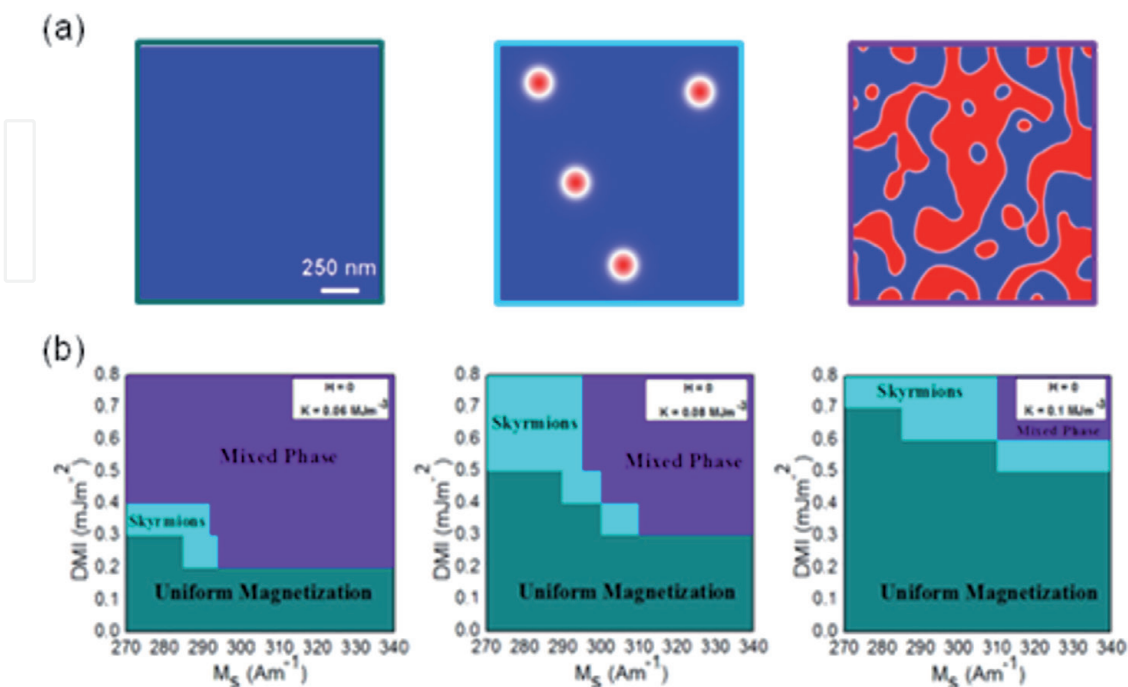


Figure 7. (a) Possible magnetic ground states. (b) DMI vs. M_s phase diagram for selected values of K . Figure adapted from reference [47].

means that both skyrmions and magnetic stripes can coexist. The phase diagrams show that for low DMI values a uniform magnetization is the preferable ground state along the entire range of saturation magnetization M_s (**Figure 7(b)**). For DMI values above 0.4 mJm^{-2} , isolated skyrmions take place, while the area that covers this magnetic state in the phase diagram expands as the saturation magnetization M_s and K values increase. On the other hand, the mixed phase exhibits an opposite behavior with a reduced area in the phase diagram when M_s and K enhances. It demonstrates that at zero magnetic field, the stability of isolated skyrmions will strongly depend on the system magnetic parameters, mainly M_s and K . Moreover, a DMI non-null value is required to stabilize isolated zero-field skyrmions, which has been achieved for both symmetric multilayers grown by MBE and magnetron sputtering techniques. Therefore, symmetric multilayers that present moderate values of DMI below 1 mJm^{-2} , with high remnant magnetization and PMA, can be strategically used to stabilize skyrmions in the absence of external magnetic field.

3. Zero-field Skyrmions in Ferrimagnetic multilayers

Ferromagnetic skyrmions have been shown remarkable phenomena under external excitation, which have helped to understand their fascinating properties. For instance, when driven by electrical current, ferromagnetic skyrmions experience a transverse motion with respect to the current direction, known as skyrmion Hall effect, which can lead to limiting their use in magnetic memory applications [50]. To overcome this issue, skyrmions have been researched in systems with antiferromagnetic coupling. It has been realized that skyrmions coupled with antiparallel magnetic moments, or, in other words, with opposite topological charges, may be used to suppress the undesirable skyrmion Hall effect when driven by electrical currents [51, 52].

In this context, materials with ferrimagnetic ordering are attractive candidates to host coupled skyrmions with opposite topological charges since they can reduce the skyrmion Hall effect due to the balance of the Magnus force acting on each skyrmion [53, 54]. In this section, we show how to observe skyrmions in lithographically shaped discs made of ferrimagnetic CoGd/Pt-based multilayer by tailoring the size of the disc diameter. For this purpose, unpatterned and patterned multilayers were grown by magnetron sputtering to image the evolution of the magnetic domain structures. **Figure 8** shows the schematic representation of the multilayer in the unpatterned and patterned (discs) geometries. The CoGd alloy was grown by using two independent Co and Gd targets in a co-sputtering deposition. The Pt/CoGd/Pt tri-layer was repeated 15 times and 2 nm Pt under and over layers were deposited as the buffer and protective oxidation, respectively. The CoGd thickness was fixed to 1.8 nm, and both unpatterned and patterned discs were deposited during the same

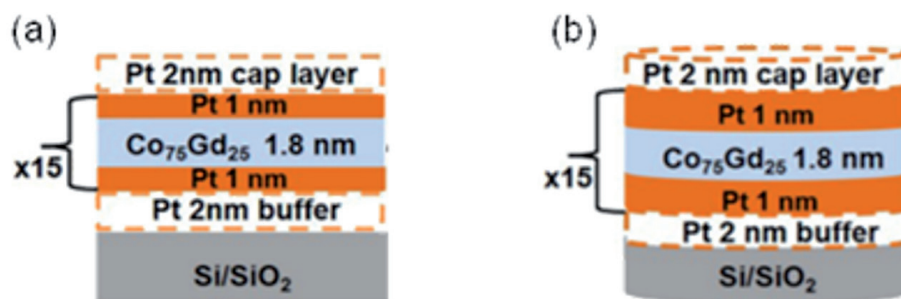


Figure 8. Representative geometries of the unpatterned (a) and patterned (b) multilayer (shaped as discs) of the CoGd/Pt multilayer. Figure adapted from [27].

sputtering batch. Electron beam lithography (EBL) was firstly performed on the Si/SiO₂ substrate to fabricate the patterned discs. More details about the methods used in the sample fabrication can be found in Ref. [27].

3.1 CoGd layer magnetic orientation

3.1.1 Magnetization behavior

As a first step, the magnetic properties of CoGd/Pt-based multilayer unpatterned sample were characterized. We used a vibrating sample magnetometer (VSM) and a SQUID to measure the hysteresis loops at ambient conditions and the temperature-dependent magnetization, respectively, as shown in **Figure 9**.

Hysteresis loops acquired by VSM at room-temperature exhibit the magnetization reversal for in-plane (IP) and out-of-plane (OOP) magnetic fields (**Figure 9(a)**). One may observe that the unpatterned CoGd multilayer presents a perpendicular magnetic anisotropy (PMA). On the other side, the out-of-plane magnetization has a tail-like structure with low remnant magnetization (blue curve) that reflects on the magnetic domain pattern observed at zero-field as it will be shown later. In **Figure 9(b)**, the temperature-dependent magnetization under zero magnetic field shows a behavior previously observed in ferrimagnetic alloys made of 3d transition metals and 4f rare earth elements. Depending on the composition between the alloy elements, the Co and Gd magnetic moments may align along the same or opposite direction, being ordered ferro- or ferrimagnetically. If the magnetic moments are arranged in an anti-parallel alignment, the compensation temperature corresponds to the magnetic moments of the Co and Gd sublattices compensating each other, leading to a minimization of the resultant magnetization [55]. This behavior is an important signature of the sample ferrimagnetic order. Starting from 2 K and without magnetic field, the sample magnetization decreases slowly as the temperature is increased, reaching a magnetization minimum at 154 K. By further increasing the temperature, the magnetization raises until reaching room-temperature (300 K), before gradually reducing around 350–400 K. This peculiar temperature-dependent behavior indicates that the CoGd/Pt based multilayer has a ferrimagnetic order of the Co and Gd magnetic moments.

3.1.2 X-ray spectroscopy and X-ray magnetic circular dichroism

X-ray absorption spectroscopy (XAS) and X-ray magnetic circular dichroism (XMCD) were performed to extract the magnetic orientation of each Co and Gd

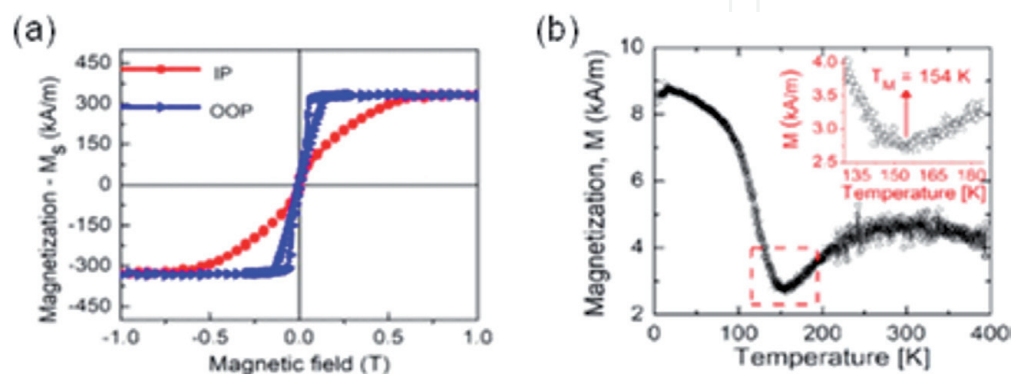


Figure 9. (a) Hysteresis loops obtained with magnetic field applied in-plane (IP) (red curve) and out-of-plane (OOP) (blue curve). (b) Temperature-dependent magnetization in the absence of magnetic field. Figure adapted from [27].

sublattice by taking advantage of the technique chemical selectivity. It allows us to further confirm the magnetic order of the CoGd alloy at room-temperature. The XAS was obtained under an out-of-plane magnetic field relative to the sample surface and parallel to the incoming X-rays by using a superconducting magnet [56]. Right and left circularly polarized X-rays were used to separate the dependent magnetic orientation of the Co and Gd elements.

Figure 10(a) shows the XAS acquired for Co around the $L_{2,3}$ absorption edges. At the first and more intense peak around 779 eV (L_3 edge), there are two distinct amplitudes: higher (dashed blue line), for left circularly polarized X-rays, and lower (solid red line), for right circularly polarized X-rays. This difference in amplitude is due to the X-ray magnetic circular dichroism that relates the dependence of the element magnetic orientation with the incoming X-ray polarization. Likewise, for Gd, a difference in amplitude is also observed at the most intense peak around 1552 eV at the Gd M_5 edge. However, contrary to the Co case, higher amplitude occurs for right circularly polarized X-rays, while lower absorption for left circularly polarized X-rays (**Figure 10(c)**). These results reflect on the XMCD (difference between the right and left circularly polarized X-ray spectra), as demonstrated in **Figures 10(b, d)**.

Looking at the L_3 and M_5 edges where the XAS maximum occurs, one can see that the XMCD is negative for Co, while it is positive for Gd. This confirms that the magnetic orientation of the Co and Gd are arranged in an antiparallel direction, thus forming a ferrimagnetic CoGd alloy at room-temperature. This result helped us to conduct the magnetic force microscopy images of the CoGd/Pt

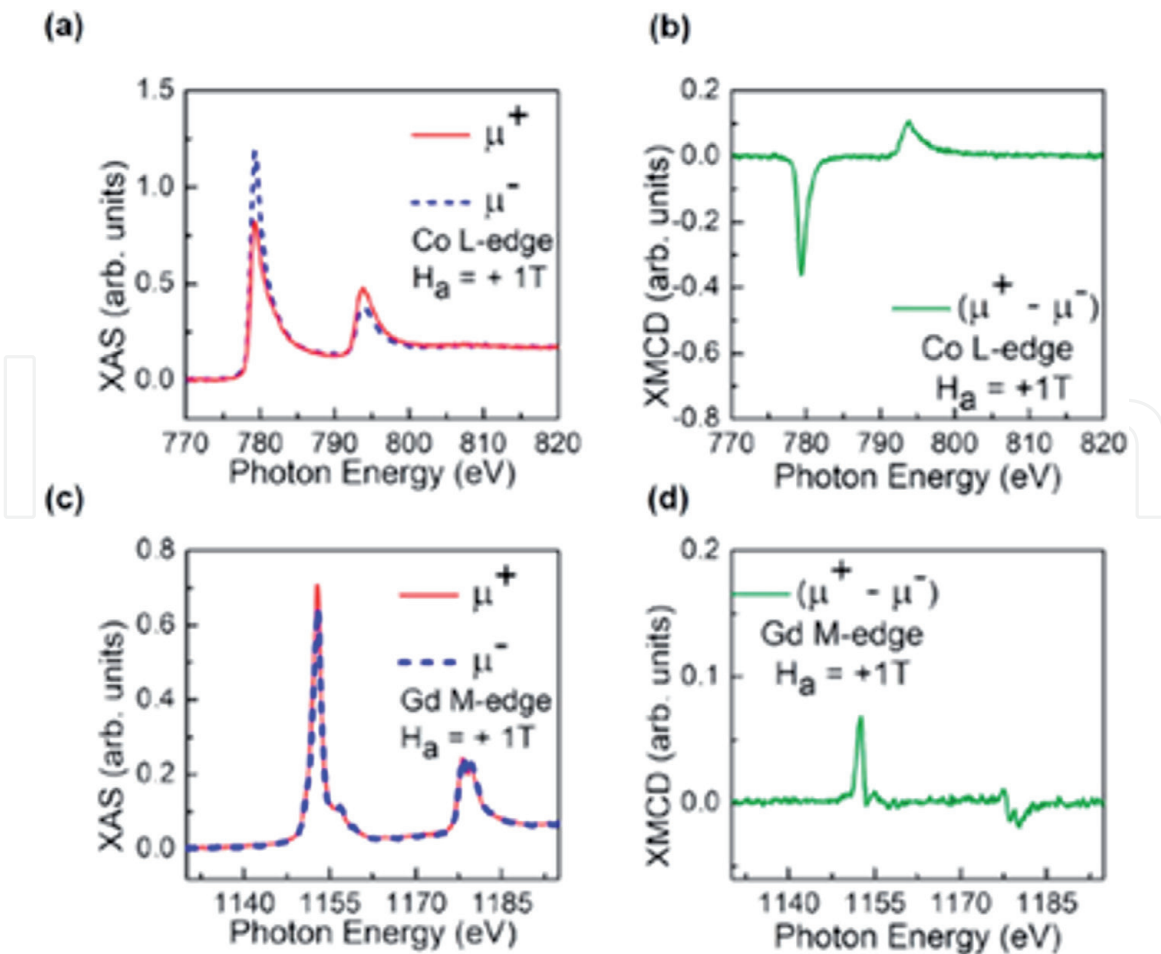


Figure 10. (a), (c) XAS acquired around the Co $L_{2,3}$ and Gd $M_{4,5}$ edges, respectively. (b), (d) XMCD acquired for Co and Gd. Figure adapted from [27].

multilayer and confirms the magnetic textures observed at ambient conditions as ferrimagnetic domains.

3.2 Magnetic textures

3.2.1 Unpatterned multilayer

Magnetic force microscopy was carried out to image the magnetic domains of the unpatterned sample and observe its features. **Figure 11(a)** shows the image acquired at remanence with alternating red and blue stripes in a typical worm-like configuration. By recalling that the out-of-plane magnetization of the unpatterned sample exhibits low remnant magnetization (see **Figure 9(a)**), it is expected to observe this type of magnetic texture in such CoGd/Pt-based multilayer.

The magnetic domain pattern is characterized by a spatial periodicity of the stripes obtained by using a linear profile on the MFM (dashed line) (**Figure 11(a)**). **Figure 11(b)** exhibits the oscillations along a 1 μm length of the spatial domain distribution of the up and down magnetic stripes, resulting in a wavelength of ~ 150 nm and domain width Δ of ~ 90 nm. The MFM image undertaken in the unpatterned multilayer will be used as a guide to evaluate the evolution of the magnetic domains in the confined structures, as will be discussed in the next section.

3.2.2 Confined nanostructures

Here we present the magnetic domain textures of the CoGd/Pt multilayer influenced by the confinement induced by the geometric disc. We produced disc arrays by electron beam lithography and lift-off techniques with different diameters of 1 μm , 650 nm, and 250 nm. **Figure 12** (top) shows the scanning electron microscopy images (SEM) of the arrays.

To visualize better the magnetic domain formation in the nanostructures, individual MFM images of the discs for each diameter are displayed at the bottom of **Figure 12**. **Figure 12** (a, bottom) displays the magnetic domain for the larger disc (1 μm). One may see that the disc supports a magnetic domain pattern like the one observed in the unpatterned multilayer (see **Figure 11(a)**), with alternating up and down magnetic stripes. Therefore, there is no significant influence of the geometric confinement at this specific diameter on the magnetic domain type formation. On the other hand, the geometric confinement leads to a modification of the magnetic stripe periodicity in the disc compared to the unpatterned sample

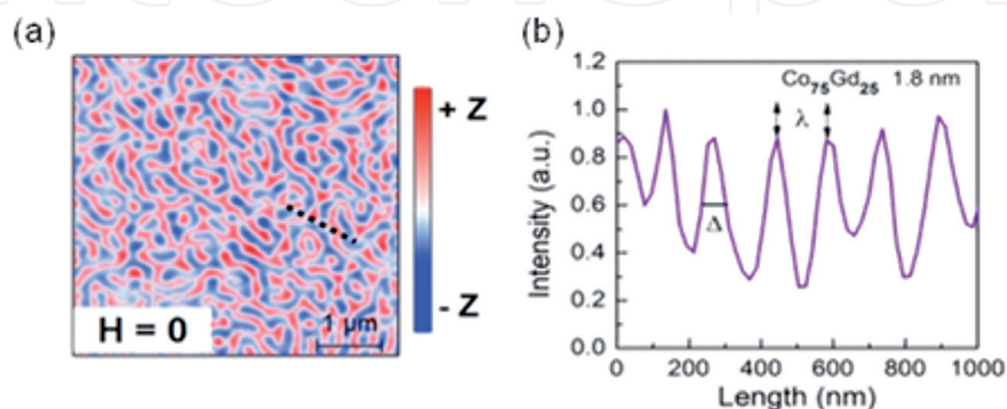


Figure 11. (a) MFM image of the unpatterned sample exhibiting magnetic stripes (blue and red) with out-of-plane orientation. (b) Domain periodicity extracted by performing line scan on the MFM image. Figure adapted from [27].

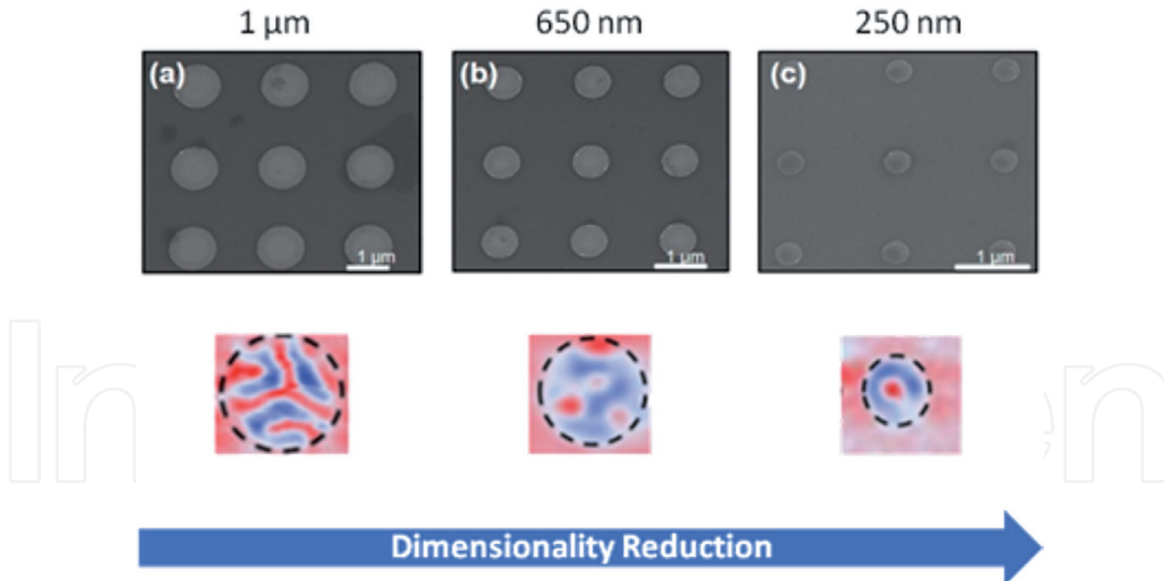


Figure 12.

(Top) Scanning electron microscopy (SEM) images of the disc arrays. (Bottom) Respective MFM images of magnetic domain textures in individual discs. (a) $1\ \mu\text{m}$, (b) $650\ \text{nm}$, (c) $250\ \text{nm}$. Figure adapted from [27].

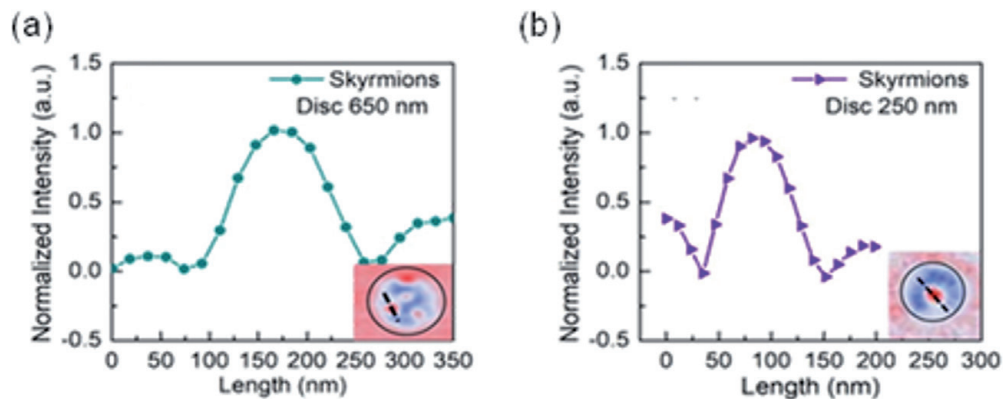


Figure 13.

Profile as a function of the length acquired by using line scan on the multiple skyrmions (a) and single skyrmions (b). Adapted from the supplementary material of reference [27].

($\sim 190\ \text{nm}$ vs. $\sim 150\ \text{nm}$, respectively). This indicates that the confinement given by the $1\ \mu\text{m}$ diameter increases the distance between up and down magnetic stripes.

The impact of the disc size is more evidenced for the $650\ \text{nm}$ diameter disc, where the confinement strongly modifies the magnetic domain pattern. The disc does not support a magnetic stripe domain, but rather the formation of small skyrmions, with a size of $\sim 120\ \text{nm}$ (**Figure 13(a)**). It is worth noting that this disc size supports three ferrimagnetic skyrmions at room-temperature and zero magnetic field. By further reducing the disc size to $250\ \text{nm}$, a stable single ferrimagnetic skyrmion is observed in the nanostructure. The single ferrimagnetic skyrmion exhibits a size of $\sim 70\ \text{nm}$ (**Figure 13(b)**), which is a very desirable feature for the use of this magnetic structure in future applications [57]. Therefore, by tailoring the disc diameter, we could stabilize magnetic domain textures at room-temperature and zero-field from magnetic stripe configurations, in larger discs, to multiple or single skyrmions in smaller discs. Furthermore, the reduction of the disc size and hence increased confinement modifies not only the magnetic domain type but also allows the existence of multiple or single ferrimagnetic skyrmions. This control can be used in new applications based on the dynamic mode of coupled skyrmions such as neuromorphic computing [58].

4. Conclusion

To summarize, in this chapter we presented two recent approaches to stabilize skyrmions at zero magnetic field and room-temperature. First, ferromagnetic skyrmions were observed in unpatterned symmetric Pd/Co/Pd multilayer by tuning both the remnant magnetization and perpendicular magnetic anisotropy. The PMA enhancement in combination with high remnant magnetization found for the thinnest Co layer (0.2 nm) yields the formation of ferromagnetic skyrmions at ambient conditions without the assistance of a magnetic field. By comparing the experimental 165 nm and simulated skyrmion sizes, we are able to estimate the non-vanishing DMI around $0.4\text{--}0.8\text{ mJm}^{-2}$, as an additional sample parameter required to stabilize skyrmions even in nominally symmetric multilayers. The DMI obtained in the micromagnetic modeling emerges mainly owing to the imperfections (roughness, intermixing) at the Co/Pd interfaces, allowing the formation of zero-field magnetic domains and isolated skyrmions.

Second, ferrimagnetic skyrmions were stabilized in confined geometric discs made of Pt/CoGd-based multilayers. The ferrimagnetic order of the multilayer is confirmed by dependent-temperature SQUID measurement and room-temperature XMCD. By adjusting the disc diameter, magnetic stripes in larger discs evolve to multiple and single ferrimagnetic skyrmions in smaller discs. The single skyrmion observed in the 250 nm diameter exhibits a size of ~ 70 nm. This sub-100 nm size and quasi antiferromagnetic arrangement of the skyrmions are very desirable both for fundamental physics understanding regarding the skyrmion Hall effect and technological applications based on antiparallel coupled skyrmions. These mechanisms are robust to find skyrmions at ambient conditions and zero-field by engineering symmetric multilayers made of ferro- or ferrimagnetic layers.

Acknowledgements

This work was supported by the Brazilian funding agencies *Fundação de Amparo à Pesquisa do Estado de São Paulo* (FAPESP) (Projects No. 2012/51198-2, 2017/10581-1; 2020/07397-7) and *Conselho Nacional de Desenvolvimento Científico e Tecnológico* (CNPq) (Projects 436573/2018-0 and 436573/2018-0). We thank the Microfabrication Laboratory of the Brazilian Nanotechnology National Laboratory (LNNano, CNPEM) for support in growing sample facilities and Laboratory of Materials and Low Temperatures of the University of Campinas (UNICAMP), for the use of VSM and SQUID techniques. We also thank the Planar Grating Monochromator (PGM) beamline at the Brazilian Synchrotron Light Laboratory (LNLS, CNPEM) for XAS and XMCD measurements.

Conflict of interest

The authors declare no conflict of interest.

IntechOpen

Author details

Jeovani Brandão¹, Marcos Vinicius Puydinger dos Santos² and Fanny Béron^{2*}

1 Brazilian Synchrotron Light Laboratory (LNLS), Brazilian Center for Research in Energy and Materials (CNPEM), Campinas, SP, Brazil

2 Gleb Wataghin Institute of Physics, University of Campinas (UNICAMP), Campinas, SP, Brazil

*Address all correspondence to: fberon@ifi.unicamp.br

IntechOpen

© 2021 The Author(s). Licensee IntechOpen. This chapter is distributed under the terms of the Creative Commons Attribution License (<http://creativecommons.org/licenses/by/3.0>), which permits unrestricted use, distribution, and reproduction in any medium, provided the original work is properly cited. 

References

- [1] A. N. Bogdanov and D. A. Yablonskii, Thermodynamically stable "vortices" in magnetically ordered crystals. The mixed state of magnets. *Sov. Phys. JETP* 68, 101 (1989).
- [2] Ryu, K.S., Thomas, L., Yang, S.H. *et al.* Chiral spin torque at magnetic domain walls. *Nature Nanotech* 8, 527533 (2013).
- [3] Emori, S., Bauer, U., Ahn, S.-M., Martinez, E. & Beach, G. S. D. Current-driven dynamics of chiral ferromagnetic domain walls. *Nat. Mater.* 12, 611 (2013).
- [4] Chen, G. *et al.* Tailoring the chirality of magnetic domain walls by interface engineering. *Nat. Commun.* 4, 2671 (2013).
- [5] Brataas, A. Chiral domain walls move faster. *Nat. Nanotech.* 8, 485 (2013).
- [6] Nagaosa, N. & Tokura, Y. Topological properties and dynamics of magnetic skyrmions. *Nat. Nanotechol.* 8, 899 (2013).
- [7] Shibata, K. *et al.* Towards control of the size and helicity of skyrmions in helimagnetic alloys by spin-orbit coupling. *Nature Nanotech.* 8, 723 (2013).
- [8] A. Hrabec, Z. Luo, L. J. Heyderman, and P. Gambardella, Synthetic chiral magnets promoted by the Dzyaloshinskii-Moriya interaction. *Appl. Phys. Lett.* 117, 130503 (2020)
- [9] Borie, B., Kehlberger, A., Wahrhusen, J., Grimm, H. & Kläui, M. Geometrical dependence of domain-wall propagation and nucleation fields in magnetic-domain-wall sensors. *Phys. Rev. Applied* 8, 024017 (2017).
- [10] J. Brandão, A. Mello, F. Garcia, L.C. Sampaio. Trajectory and chirality of vortex domain walls in ferromagnetic nanowires with an asymmetric branch. *J. Appl. Phys.*, 121, 093905 (2017).
- [11] B. Borie, J. Wahrhusen, H. Grimm, M. Kläui. Geometrically enhanced closed-loop multi-turn sensor devices that enable reliable magnetic domain wall motion. *Appl. Phys. Lett.* 111, 242402 (2017).
- [12] Allwood, D. A. *et al.* Magnetic domain wall logic. *Science* 309, 1688 (2005).
- [13] Currivan-Incorvia, J. A. *et al.* Logic circuit prototypes for three-terminal magnetic tunnel junctions with mobile domain walls. *Nat. Commun.* 7, 10275 (2016).
- [14] Luo, Z., Hrabec, A., Dao, T.P. *et al.* Current-driven magnetic domain-wall logic. *Nature* 579, 214 (2020).
- [15] Parkin, S. S. P., Hayashi, M. & Thomas, L. Magnetic domain-wall racetrack memory. *Science* 320, 190 (2008).
- [16] Tomasello, R., Martinez, E., Zivieri, R. *et al.* A strategy for the design of skyrmion racetrack memories. *Sci Rep* 4, 6784 (2014).
- [17] R. D. McMichael, M. J. Donahue. Head to head domain walls structures in thin magnetic stripes. *IEEE Trans. Magn.* 33, 4167 (1997).
- [18] T. Shinjo *et al.*, Magnetic vortex observation in circular dots. *Science* 289, 930 (2000).
- [19] U. K. Rößler, A. N. Bogdanov, C. Pfleiderer, Spontaneous skyrmion ground states in magnetic metals. *Nature* 442, 797 (2006).
- [20] Moreau-Luchaire, C. *et al.* Additive interfacial chiral interaction in multilayers for stabilization of small

individual skyrmions at room temperature. *Nat. Nanotech.* 11, 444 (2016).

[21] Upadhyaya, P.; Yu, G.; Amiri, P. K.; Wang, K. L. Electric-Field Guiding of Magnetic Skyrmions. *Phys. Rev. B: Condens. Matter Mater. Phys.* 2015, 92, 134411.

[22] Ogawa, N., Seki, S. & Tokura, Y. Ultrafast optical excitation of magnetic skyrmions. *Sci. Rep.* 5, 9552 (2015).

[23] Woo, S. *et al.* Observation of room temperature magnetic skyrmions and their current-driven dynamics in ultrathin metallic films. *Nat. Mater.* 15, 501 (2016).

[24] Bogdanov, A. N. & Röbber, U. K. Chiral symmetry breaking in magnetic thin films and multilayers. *Phys. Rev. Lett.* 87, 037203 (2001).

[25] Zhang, S. *et al.* Topological computation based on direct magnetic logic communication. *Sci. Rep.* 5, 15773 (2015).

[26] Senfu Zhang *et al.* *New J. Phys.* 17, 023061 (2015).

[27] Brandão, J., Dugato, D. A., Puydinger dos Santos, M. V. & Cezar, J. C. Evolution of zero-field ferrimagnetic domains and skyrmions in exchange-coupled Pt/CoGd/Pt confined nanostructures: implications for antiferromagnetic devices. *ACS Appl. NanoMater.* 2, 7532 (2019).

[28] Cortés-Ortuño, D., Wang, W., Beg, M. *et al.* Thermal stability and topological protection of skyrmions in nanotracks. *Sci. Rep.* 7, 4060 (2017).

[29] Fert, A., Cros, V. & Sampaio, J. Skyrmions on the track. *Nature Nanotech.* 8, 152 (2013).

[30] Meyer, S., Perini, M., von Malottki, S. *et al.* Isolated zero field sub-10 nm

skyrmions in ultrathin Co films. *Nat Commun.* 10, 3823 (2019).

[31] Mühlbauer, S. *et al.* Skyrmion lattice in a chiral magnet. *Science* 323, 915 (2009).

[32] Yu, X. Z. *et al.* Real-space observation of a two-dimensional skyrmion crystal. *Nature* 465, 901 (2010).

[33] Yu, X. Z. *et al.* Near room-temperature formation of a skyrmion crystal in thin-films of the helimagnet FeGe. *Nat. Mater.* 10, 106 (2011).

[34] Dzialoshinskii, I. E. Thermodynamic theory of “weak” ferromagnetism in antiferromagnetic substances. *Sov. Phys. JETP* 5, 1259(1957).

[35] Soumyanarayanan, A., Raju, M., Gonzalez Oyarce, A. *et al.* Tunable room-temperature magnetic skyrmions in Ir/Fe/Co/Pt multilayers. *Nature Mater.* 16, 898 (2017).

[36] Fert, A., Reyren, N. & Cros, V. Magnetic skyrmions: advances in physics and potential applications. *Nat. Rev. Mater.* 2, 17031 (2017).

[37] Hervé, M., Dupé, B., Lopes, R. *et al.* Stabilizing spin spirals and isolated skyrmions at low magnetic field exploiting vanishing magnetic anisotropy. *Nat Commun.* 9, 1015 (2018).

[38] Romming, N., Kubetzka, A., Hanneken, C., von Bergmann, K. & Wiesendanger, R. Field-dependent size and shape of single magnetic skyrmions. *Phys. Rev. Lett.* 114, 177203 (2015).

[39] Boulle, O. *et al.* Room-temperature chiral magnetic skyrmions in ultrathin magnetic nanostructures. *Nat. Nanotechnol.* 11, 449 (2016).

[40] Yu, G. *et al.* Room-temperature skyrmions in an antiferromagnet-based

heterostructure. *Nano Lett.* 18, 980 (2018).

[41] Zhang, S. *et al.* Direct writing of room temperature and zero field skyrmion lattices by a scanning local magnetic field. *Appl. Phys. Lett.* 112, 132405 (2018).

[42] Guang, Y., Bykova, I., Liu, Y. *et al.* Creating zero-field skyrmions in exchange-biased multilayers through X-ray illumination. *Nat Commun.* 11, 949 (2020).

[43] Yao Guang, Yong Peng, Zhengren Yan, Yizhou Liu, Junwei Zhang, Xue Zeng, Senfu Zhang, Shilei Zhang, David M. Burn, Nicolas Jaouen, Jinwu Wei, Hongjun Xu, Jiafeng Feng, Chi Fang, Gerrit Laan, Thorsten Hesjedal, Baoshan Cui, Xixiang Zhang, Guoqiang Yu, Xiufeng Han. *Electron Beam Lithography of Magnetic Skyrmions. Advanced Materials*, 32, 2003003 (2020).

[44] Pollard, S. D. *et al.* Observation of stable Néel skyrmions in Co/Pd multilayers with Lorentz transmission electron microscopy. *Nat. Commun.* 8, 14761-14761 (2017).

[45] A. Hrabec, N. A. Porter, A. Wells, M. J. Benitez, G. Burnell, S. McVitie, D. McGruther, T. A. Moore, and C. H. Marrows, *Phys. Rev. B* 90, 020402 (2014).

[46] A. V. Davydenko, A. G. Kozlov, A. G. Kolesnikov, M. E. Steblyi, G. S. Suslin, Y. E. Vekovshinin, A. V. Sadovnikov, and S. A. Nikitov, Dzyaloshinskii-Moriya interaction in symmetric epitaxial Co/Pd (111)_xN superlattices with different numbers of Co/Pd bilayers, *Phys. Rev. B* 99, 014433 (2019).

[47] Brandão, J., Dugato, D.A., Seeger, R.L. *et al.* Observation of magnetic skyrmions in unpatterned symmetric multilayers at room temperature and

zero magnetic field. *Sci. Rep.* 9, 4144 (2019).

[48] Liu, Z. *et al.* Thickness dependent magnetization dynamics of perpendicular anisotropy Co/Pd multilayer films. *J. Magn. Magn. Mater.* 323, 1623 (2011).

[49] Behera, A. K. *et al.* Size and shape of skyrmions for variable Dzyaloshinskii Moriya interaction and uniaxial anisotropy. *J. Phys. D: Appl. Phys.* 51, 285001 (2018).

[50] Jiang, W. *et al.* Direct observation of the skyrmion Hall effect. *Nature Phys.* 13, 162 (2016).

[51] Zhang, X. *et al.* Antiferromagnetic Skyrmion: Stability, Creation and Manipulation. *Sci. Rep.* 6, 24795 (2016).

[52] Haiyan Xia *et al.* Control and manipulation of antiferromagnetic skyrmions in racetrack. *J. Phys. D: Appl. Phys.* 50, 505005 (2017).

[53] Buttner, F., Lemesh, I. Beach, G. S. D. Theory of isolated magnetic skyrmions: From fundamentals to room temperature applications. *Sci. Rep.* 8, 4464 (2018).

[54] Woo, S. *et al.* Current-driven dynamics and inhibition of the skyrmion Hall effect of ferrimagnetic skyrmions in GdFeCo films. *Nat. Commun.* 9,959 (2018).

[55] Caretta, L; *et al.* Fast current-driven domain walls and small skyrmions in a compensated ferrimagnet. *Nat. Nanotechnol.* 13, 1154-1160 (2018).

[56] Cezar, J. C.; *et al.* The U11 PGM beam line at the Brazilian National Synchrotron Light Laboratory. *J. Phys.: Conf. Ser.* 425, 072015 (2013).

[57] Navau, C.; Del-Valle, N.; Sanchez, A. Analytical trajectories of skyrmions in confined geometries: Skyrmionic

racetracks and nanooscillators. *Phys. Rev. B: Condens. Matter Mater. Phys.* **94**, 184104 (2016).

[58] Torrejon, J.; Riou, M.; Araujo, F. A.; Tsunegi, S.; Khalsa, G.; Querlioz, D.; Bortolotti, P.; Cros, V.; Yakushiji, K.; Fukushima, A.; Kubota, H.; Yuasa, S.; Stiles, M. D.; Grollier, J. Neuromorphic computing with nanoscale spintronic oscillators. *Nature*, **547**, 428 (2017).

IntechOpen